JOURNAL OF GEOPHYSICAL RESEARCH, VOL. 112, B06408, doi:10.1029/2006JB004357, 2007

Frontal accretion: An internal clock for bivergent wedge deformation and surface uplift

S. Hoth,[1] A. Hoffmann-Rothe,[2] and N. Kukowski[1]

Received 20 February 2006; revised 23 November 2006; accepted 31 January 2007; published 13 June 2007.

[1] We propose a conceptual model of frontal accretion within bivergent wedges, which is based on two-dimensional sandbox simulations and the analysis of particle displacement fields. Each frontal accretion cycle consists of a thrust initiation, an underthrusting phase, and a reactivation phase. The location and magnitude of deformation within a bivergent wedge and its associated surface uplift vary systematically with the phase of the frontal accretion cycle and are thus predictable. Therefore the frontal accretion cycle can be considered as an internal clock for wedge-scaled deformation and surface uplift. We further demonstrate that the geometry of the deformation front and the spatial distribution of surface uplift can be used to infer the currently active phase within a frontal accretion cycle. Surface uplift of the axial zone and the retrowedge may reach up to half of the thickness of the incoming sedimentary layer during a frontal accretion cycle. We estimate cycle duration to range between 10^4 and 10^5 years, which is thus similar to the time frame of climatic cycles. The proposed conceptual model provides an explanation for the commonly observed transience of deformation and surface uplift and for the discrepancy between geodetic, paleoseismologic, and geologic estimates of fault slip.

Citation: Hoth, S., A. Hoffmann-Rothe, and N. Kukowski (2007), Frontal accretion: An internal clock for bivergent wedge deformation and surface uplift, *J. Geophys. Res.*, *112*, B06408, doi:10.1029/2006JB004357.

1. Introduction

[2] Bivergent wedges operate at several spatial scales, i.e., at the scale of entire orogenic belts such as the European Alps [*Pfiffner et al.*, 2000] and the Pyrenees [*Choukroune*, 1989]; at the scale of fold and thrust belts like the Sierras Pampeanas [*Cristallini et al.*, 2004]; and at the scale of accretionary prisms, such as the Sunda Arc [*Silver and Reed*, 1988], the Mediterranean Ridge [*Le Pichon et al.*, 2002], Barbados [*Speed*, 1990], and the Nankai accretionary prism [*Taira et al.*, 1991].

[3] The kinematic evolution of bivergent wedges results from the (partial) subduction of continental or oceanic lithosphere and accretion of crustal material. According to *Willett et al.* [1993], a velocity discontinuity (singularity) separates the downgoing plate from the overriding plate, thus marking the lower limit of accretion (Figure 1a). The asymmetry of the convergence geometry causes a polarity in the crustal mass transfer; that is, all crustal mass delivered into a bivergent wedge is derived from the downgoing plate. Thereby two crustal subwedges form. The prowedge, located upstream of the singularity, grows by frontal and basal accretion of lower plate material. In contrast, the retrowedge, located downstream of the singularity, develops by translation of prowedge material above the retroshear zone and by frontal accretion of upper plate material during later stages of convergence [*Willett et al.*, 1993; *Beaumont et al.*, 1996]. The axial zone is defined as the topographic culmination of a bivergent wedge.

[4] The subduction-accretion process described above leads to the formation of a bivergent wedge with a geometry controlled by the basal and internal mechanical properties [*Platt*, 1986; *Willett et al.*, 1993; *Beaumont et al.*, 1994; *Willett et al.*, 2001]. A Coulomb-type rheology, which is pressure-dependent and strain rate-independent, appears to satisfactorily describe the mechanical behavior of brittle, upper crustal rocks. The key physical assumption implicit in the critical Coulomb wedge (CCW) concept is that the wedge is at failure everywhere and thus in a critical mechanical state. A critically tapered wedge slides stably over its base without internal deformation and grows self similarly [*Davis et al.*, 1983; *Dahlen*, 1990].

[5] Previous research on bivergent wedge evolution has focused on the link between the shape of, and the mechanics within, bivergent wedges in terms of surface processes, the mechanical stratification of the incoming layer and the sequence of thrusting, i.e., forward breaking, break-back or synchronous thrusting [*Malavieille*, 1984; *Beaumont et al.*, 1996; *Willett*, 1999; *Storti et al.*, 2000; *Naylor et al.*, 2005; *Hoth et al.*, 2006]. Although the CCW concept and the concept of thrust sequences [*Boyer and Elliott*, 1982; *Butler*, 1987; *Morley*, 1988; *Boyer*, 1992; *Butler*, 2004] have significantly improved our understanding of mountain building, both concepts are limited with respect to their

[1]GeoForschungsZentrum Potsdam, Potsdam, Germany.
[2]Bundesanstalt für Geowissenschaften und Rohstoffe, Hannover, Germany.

0148-0227/07/2006JB004357$09.00

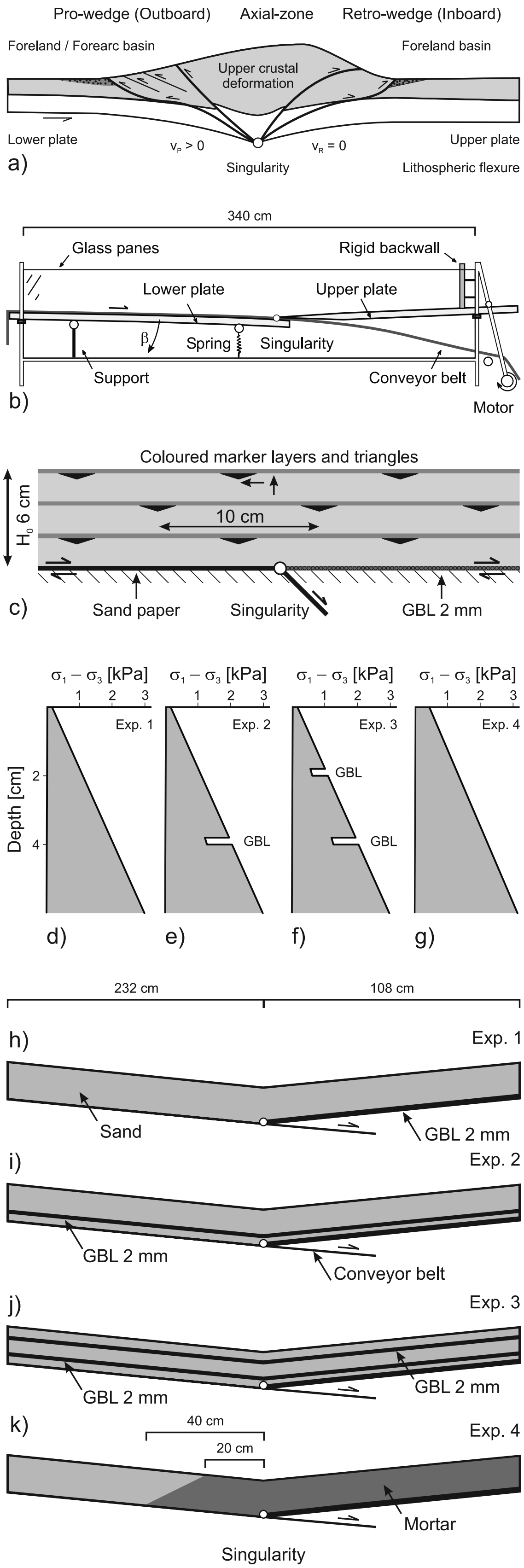

Figure 1. (a) Schematic bivergent wedge. (b) Sketch of the experimental device with internal dimensions (length, width, height) of 340 × 21 × 60 cm. For details and discussion on the influence of the setup on model evolution, please see *Hoth et al.* [2006] and *Schreurs et al.* [2006]. (c) Mechanical stratigraphy of reference experiment 1. (d–g) Calculated strength profiles for the mechanic stratigraphies used in the experiments. Strength profile in Figure 1g was calculated for mortar. (h–k) Position and distribution of glass bead layer and mortar for different experiments. Basal friction was the same in all experiments. GBL is glass bead layer. Basal accretion by duplex formation occurs beneath, frontal accretion by thrust imbrication occurs above the lowest GBL. For further details on the experimental setup and its influence on model evolution, please see the auxiliary material.

ability (1) to link the long-term evolution of bivergent wedges with the short-term variability of slip accumulation and (2) to predict the spatiotemporal distribution of deformation within and the surface uplift of a bivergent wedge. Thus a better understanding of bivergent wedge evolution would not only guide our perspective of the geological record, but would also help to constrain seismic and landslide hazard assessment studies within actively deforming regions. Recently, *Gutscher et al.* [1998] and *Hoffmann-Rothe et al.* [2004] demonstrated that frontal accretion consists of two principle phases, that may control the spatiotemporal distribution of deformation and surface uplift: (1) a short thrust initiation phase, marked by the formation of a thrust imbricate within the prolayer and (2) an underthrusting phase, during which the material is underthrust beneath the wedge.

[6] On the basis of these results we aim to elucidate the spatiotemporal evolution of strain partitioning within, and the associated surface uplift of, bivergent wedges by employing two-dimensional (2-D) sandbox simulations. Thereby, special emphasis is devoted to the identification of process chains. Finally, we propose a conceptual model for frontal accretion cycles within bivergent wedges. We demonstrate that this conceptual model (1) provides the ability to predict the timing, magnitude and location of deformation and surface uplift within bivergent wedges, (2) explains the occurrence of forward breaking, synchronous- and out-of-sequence thrusting, and (3) thus links the long-term evolution of bivergent wedges with the short-term variability of slip accumulation.

2. Methodological Approach

[7] Scaled 2-D sandbox simulations in conjunction with particle image velocimetry (PIV, section 2.2) are used to identify spatial and temporal patterns of deformation within, and surface uplift of, bivergent wedges. Granular flow of sieved, dry quartz sand is characterized by a strain-dependent deformation behavior with prefailure strain hardening and postfailure strain softening, similar to the nonlinear deformation behavior of crustal rocks in the brittle field [*Mandl et al.*, 1977; *Lohrmann et al.*, 2003]. The observed similarity between the mechanical properties of sand (Table 1) and

Table 1. Physical Properties of Analogue Materials Used in Experiments[a]

Material	Type	Grain Size, μm	Density, g/cm^3	ϕ_{peak},[b] deg	C_{peak}, Pa	ϕ_{static},[c] deg	C_{static}, Pa	ϕ_{dyn},[d] deg	C_{dyn}, Pa	Strain Softening,[e]
Sand	Internal	20–630	1.74 ± 0.01	35.36 ± 0.34	43.47 ± 44.34	29.82 ± 0.19	176.38 ± 24.80	28.20 ± 0.05	94.66 ± 6.53	20.24
Glass beads	Internal	300–400	1.59 ± 0.01	29.14 ± 0.14	−6.13 ± 18.82	25.91 ± 0.09	78.89 ± 11.56	22.51 ± 0.04	42.71 ± 5.15	13.63
Mortar	Internal	145–1250	1.82 ± 0.03	34.09 ± 0.15	118.89 ± 20.54	35.18 ± 0.59	164.71 ± 77.27	31.38 ± 0.22	53.77 ± 28.95	7.95
Sand paper	Basal[f]	<400	–	32.02 ± 0.32	−63.09 ± 42.49	30.34 ± 0.07	61.37 ± 8.73	28.62 ± 0.15	65.98 ± 19.77	–

[a]Internal properties were measured with sieved materials; basal properties were determined relative to sieved sand. Interpolation of the Mohr envelopes was used to calculate cohesion. The sand, S30T in industry standards, was washed and dried at high temperature by the mining company before delivery to the laboratory.

[b]Peak friction provides the strength of undeformed material.

[c]Static stable friction provides the strength of previously deformed material.

[d]Dynamic stable friction provides the strength of active shear zones [*Byerlee*, 1978].

[e]Strain softening expresses the percentage difference between peak friction and dynamic stable friction.

[f]Basal friction was measured with respect to the sand.

crustal rocks in the brittle regime, and the scale invariance of brittle behavior justifies the application of laboratory sand wedges to investigate the kinematics and dynamics of accretionary wedges, fold-and-thrust belts, and bivergent orogens. It further supports the application of the CCW concept, which assumes a Mohr-Coulomb type rheology, to laboratory sand wedges [*Davis et al.*, 1983; *Malavieille*, 1984; *Wang and Davis*, 1996; *Gutscher et al.*, 1998; *Storti et al.*, 2000]. Following *Hubbert* [1937], a geometric scaling factor of 10^5 was calculated; that is, 1 cm in the model corresponds to $\sim$1 km in nature. This scaling approach is commonly used for sandbox simulations [e.g., *Storti et al.*, 2000; *Kukowski et al.*, 2002; *Hampel et al.*, 2004] and requires that all experiments are conducted under normal gravity conditions.

2.1. Experimental Setup

[8] The sandbox simulations were performed in a glass-sided deformation apparatus, which was introduced by *Hoth et al.* [2006]. It consists of upper and lower elastic wooden plates, which overlap in the center, and are only fixed at their respective outward sides to allow for load driven flexure. The lower plate is supported by a spring to adjust its stiffness. The corresponding dip angle β changes from about 5° to about 7° during experimental runs. In order to minimize the influence of the rigid back wall on model evolution, the singularity is located at a sufficient distance (Figure 1b).

[9] A key model assumption is that the mechanical energy delivered into a bivergent wedge is derived from the basal pull or drag of the subducting plate [*Silver and Reed*, 1988]. Accordingly, lower plate subduction and basal shear is simulated by a conveyor belt, which covers only the lower plate and is drawn by a motor (9 cm/min) beneath the tip of the upper plate. A sand paper with a grain size <0.4 cm was chosen for the conveyor belt, to ensure a strong mechanical coupling between the conveyor belt and the sand layer. The respective basal friction was measured using a ring shear device (Table 1). It is in the same range as published values for similar experimental devices [*Wang and Davis*, 1996; *Kukowski et al.*, 2002]. A lower basal friction would have resulted in lower and wider bivergent sand wedges.

[10] The most general and simplest scenario was used as reference experiment, i.e., collision of material with the same thickness (6 cm) and with the same mechanical properties on both sides of the singularity (Figures 1c, 1d, and 1h). Neither the wedge shape of foreland deposits [e.g., *DeCelles and Giles*, 1996] nor inherited zones of weakness commonly found in orogenic forelands were taken into account. Variation of these initial conditions would only modify the spacing of thrusts [*Bombolakis*, 1986; *Boyer*, 1995; *Hardy et al.*, 1998; *Marshak*, 2004].

[11] Subsequently, results from the reference experiment were compared with the results from three additional experiments with different mechanic stratigraphies. In two experiments dry glass beads, with significantly lower frictional properties (Table 1) were used to simulate weak layers and thus possible internal detachments (Figures 1c, 1f, 1i, and 1j). Introduction of weak layers promotes the coeval occurrence of frontal and basal accretion, as observed in several bivergent wedges, e.g., the Pyrenees and the European Alps

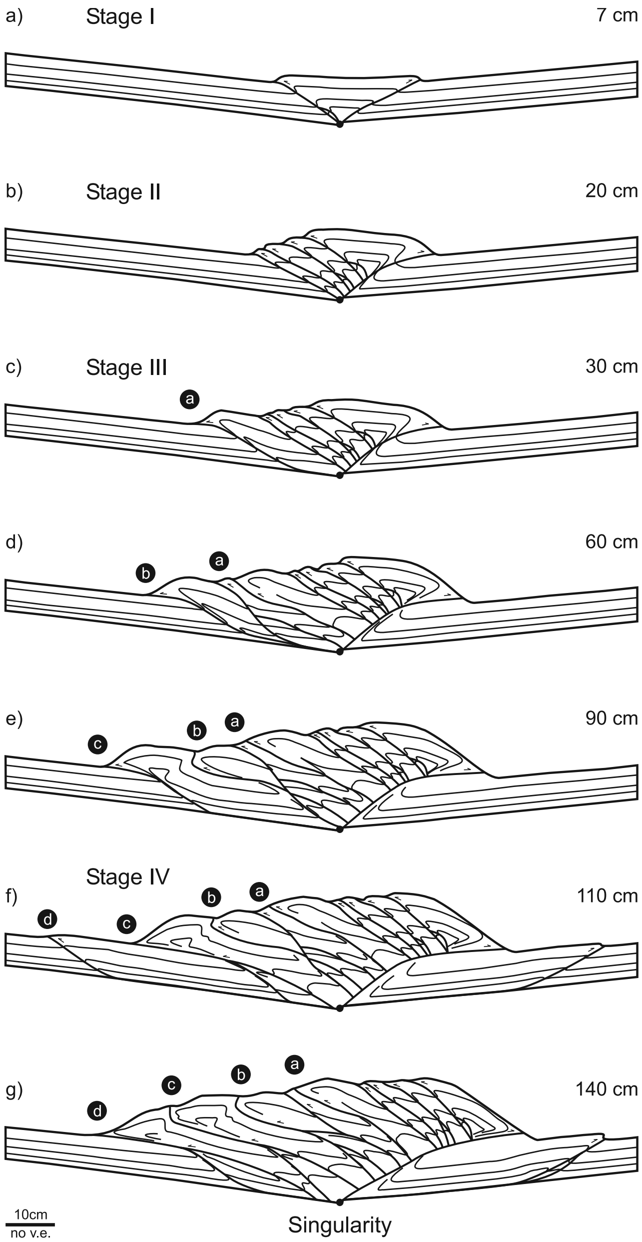

Figure 2. Line drawings of sequential evolutionary stages of the reference experiment 1. Numbers on the right are centimeters of convergence. Frontal accretion within the retrowedge occurs after ~100 cm of convergence (stage IV). Labels a to d denote thrusts; "no v.e." is no vertical exaggeration.

[*Choukroune*, 1989; *Pfiffner et al.*, 2000]. According to *Kukowski et al.* [2002] an internal glass bead layer serves only as a detachment if its internal strength is lower than the strength along the basal detachment. This imposed a further constraint to choose a high basal friction, as mentioned above. In an additional experiment, a strength contrast between the upper (mortar) and the lower plate (sand) was simulated (Figures 1g and 1k).

[12] Convergence in all four experiments was on the order of 150 cm (~150 km in nature). To promote frontal accretion within the retrowedge, the upper plate base was covered with a glass bead layer, in all experiments (see also *Pfiffner et al.* [2000] and *Hoth et al.* [2006] for further discussion on this issue). Finally, the initial model set up resembles the conditions used in other numerical and physical simulations [e.g., *Willett*, 1999; *Storti et al.*, 2000] and mimics the geometry of published sections through the Pyrenees, the European Alps and the German Variscides [*Choukroune*, 1989; *Pfiffner et al.*, 2000; *Schäfer et al.*, 2000].

2.2. Data Acquisition With PIV

[13] All experiments were monitored in cross section with two high-speed, high-resolution digital cameras to image the particle flow in the sand wedge [*Hampel et al.*, 2004; *Adam et al.*, 2005; *Hoth et al.*, 2006]. Images were taken every 1 s, except in experiment 2, where a sampling rate of 2 s was used. On the basis of an adaptive cross correlation algorithm, successive images were compared and the incremental particle displacement field as well as its derivation, the incremental horizontal shear strain e_{xy} was calculated. Visualization of the latter allows the detection of strain accumulation patterns in time and space. The accuracy of the displacement measurement is ~0.5 mm, which is similar to the size of the sand grains used. Furthermore, digital PIV images provide an excellent opportunity to extract time series for geometric features such as the propagation of deformation, the height above the singularity, the spatial distribution of surface uplift, and the displacement of thrusts. These data were derived from every fifth image, which corresponds to a convergence interval of 0.75 cm (experiment 2 1.5 cm). All geometric data derived from PIV analysis were normalized with respect to H_0, the height of the undeformed multilayer, to account for minor variations in its thickness.

[14] Edge effects are minimized through application of a low friction polymer coating the glass panes. After completion of an experiment, the sand wedge can be moistened and sectioned to examine the internal structure and control the degree of edge effects, which were found to be negligible in the experiments presented here. Reproducibility was confirmed by comparison of different data sets, i.e., propagation of deformation, surface uplift, strain accumulation of individual structures, with the ones derived from similar experimental series or repeated experiments. Finally, two conventions are made: The term proshear is used for all shear zones dipping toward the upper plate, whereas shear zones with retroshear dip toward the lower plate. The term retroshear zone is used only for the shear zone bounding the retroside of the initial pop up.

3. Experimental Results

[15] Section 3.1. provides an account of the kinematic evolution of the reference experiment. A description of the three additional experiments, with different mechanical stratigraphies is available in the auxiliary material.[1]

3.1. Kinematic Evolution of a Bivergent Sand Wedge

[16] On the basis of visual inspection of the reference experiment, the kinematic evolution of a bivergent sand

[1]Auxiliary materials are available in the HTML. doi:10.1029/2006JB004357.

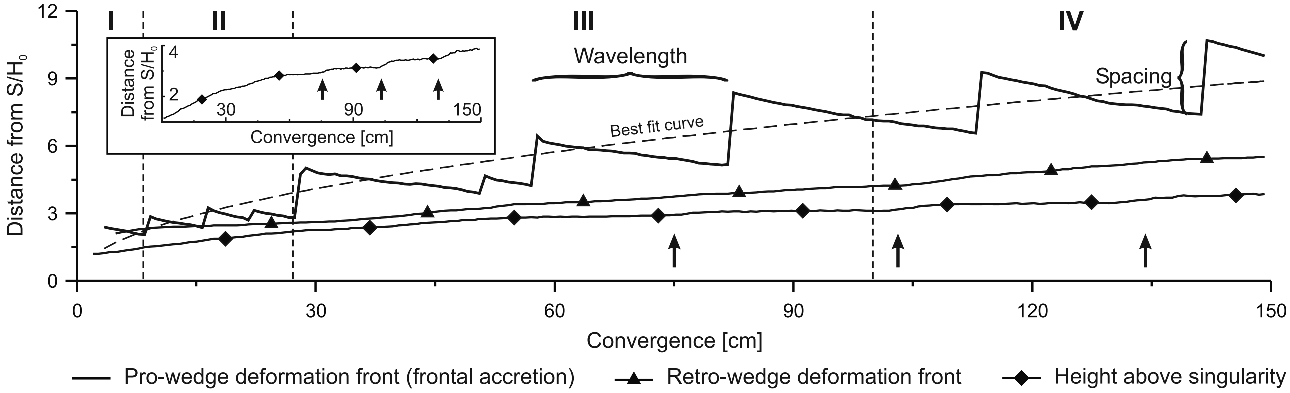

Figure 3. Evolution of geometric parameters taken from the PIV images at every 0.75 cm of convergence. All lengths are horizontal distances measured from the singularity (S). H_0 is thickness of incoming layer. Arrows point to times of accelerated vertical growth, which predate the formation of a new thrust within the prolayer. Inset shows magnification of this curve (height above the singularity) to highlight the above changes. Dashed line is the best fit curve for the propagation of deformation of frontal accretion within the prowedge: $y = 0.79\ t^{0.48}$ with $R^2 = 0.88$; y is the normalized distance between the deformation front of frontal accretion within the prowedge and the singularity and t is convergence [cm]. Roman letters and vertical dotted lines indicate duration of the four stages of bivergent wedge evolution. Graphic definition of spacing: the horizontal distance between the previous and the newly formed deformation front. Graphic definition of wavelength: the time in cm convergence between two successive thrust initiations. Note that the aspect ratio of the thrust imbricates is ~3:1.

wedge can be divided into four stages. In stage I, initial layer parallel shortening leads to the formation of two conjugate shear zones, which nucleate at the singularity and define a symmetric pop-up (Figure 2a). Further convergence leads to rapid surface uplift associated with progressive back tilting of this pop-up toward the upper plate.

[17] During stage II, three narrowly spaced thrust faults form successively within the prolayer (Figure 2b). They nucleate at the singularity and are passively carried backward and upward in the hanging wall of the retroshear zone throughout the remaining experiment. Hence this stage marks the transition from a symmetric to an asymmetric topographic and kinematic state. Surface uplift rates of the axial zone and the retrowedge are still high but start to decrease (Figure 3), while rates of thrusting along the retroshear zone remain constant.

[18] After ~30 cm of convergence (Figure 2c), the axial zone and the retrowedge provide sufficient load to initiate a basal detachment, which ramps up through the prolayer to finally form a flat-topped box anticline (stage III). Lateral growth of the prowedge is now attained by a forward breaking sequence of flat-topped box anticlines, which is hereafter referred to as frontal accretion. The basal detachment is located within the lowermost part of the prolayer, a few millimeters above the conveyor belt. During stage III, rates of the lateral growth of the prowedge, as well as surface uplift rates of the axial zone and the retrowedge decrease further (Figure 3). The latter is additionally disturbed by discrete, short-lived accelerations, which predate the formation of a new thrust within the prolayer.

[19] After ~100 cm of convergence, frontal accretion within the retrowedge takes place and hence marks the onset of stage IV. Continued convergence is now taken up by two frontal accretion systems (Figures 2f and 2g), indicating that the wedge starts to regain its initial symmetric conditions. This results in a further slowdown of the lateral growth rate of the prowedge (Figure 3).

[20] It is finally noted that the propagation of deformation within the prowedge is attained by cyclic frontal accretion. The resulting lateral growth of the prowedge (Figure 3) is proportional to the convergence (t) by $t^{0.48}$ ($R^2 = 0.88$), which is close to the theoretically predicted value of $t^{0.5}$ [*Dahlen*, 1990].

3.2. Topographic Evolution

[21] Given an Eulerian reference frame, two domains of the spatiotemporal distribution of incremental surface uplift (ISU) are distinguished within the bivergent sand wedge. The first comprises the prowedge and the second includes the axial zone and the retrowedge. ISU in the prowedge is highly variable and shows discrete accelerations, whereas the retrowedge is characterized by an almost concentric growth (Figure 4a).

[22] A more detailed insight into the topographic evolution can be derived from ISU maps: Time lines show the high spatial variability, location lines the high temporal variability of ISU for a given time interval or position in an Eulerian reference frame (Figure 4b). The initiation of individual flat-topped box anticlines is associated with a maximum ISU right above the respective ramp segment. Thus propagation of these ISU maxima through time and space reflects the propagation of deformation within the prowedge. While convergence proceeds, new thrust faults are formed and older ones are abandoned. This is coeval with a decay of ISU for a given ramp segment. However, almost all ramp segments identified in Figures 4b and 4c show a renewed increase in ISU, which can gain an order of magnitude, suggesting thus the reactivation of these ramp segments.

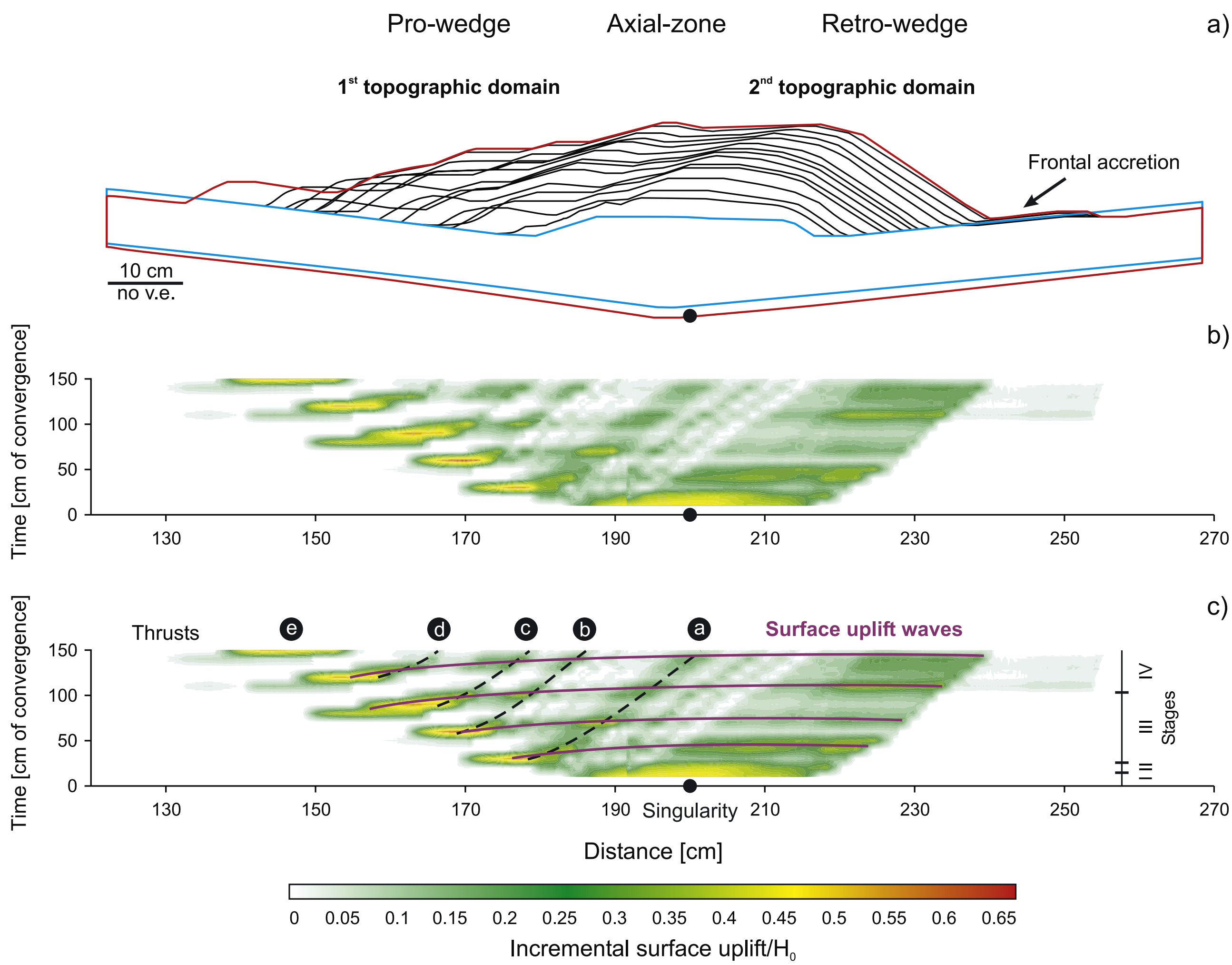

Figure 4. (a) Topographic evolution of reference experiment. Outlines were taken at every 10 cm. of convergence. The blue and red outlines denote 10 and 150 cm of convergence indicating the magnitude of flexure. Two topographic domains mirroring two different growth modes can be distinguished: (1) Cyclic accretion within the prowedge results in distinct topographic steps, (2) whereas continuous addition of prowedge derived material to the axial zone and the retrowedge leads to nearly concentric growth. (b) Incremental surface uplift of reference experiment, raw data. Note that incremental surface uplift is derived from 10 cm convergence intervals. (c) Dashed lines (black) follow surface uplift traces of ramp segments of fore thrusts. Reactivation of thrusts can result in an increase of ISU by one order of magnitude. For location of thrusts a to d see Figure 2g. Bold lines (purple) follow surface uplift waves, which are tightly linked with the accretion cycle. Roman letters denote four stages in bivergent wedge evolution (see Figures 2 and 3).

[23] Furthermore, the initiation of each thrust within the prolayer is associated with the highest ISU magnitudes right above the ramp segment and low ISU magnitudes within the axial zone and the retrowedge. With convergence, this maximum migrates as a decaying wave through the entire wedge until it has reached the tip of the retrowedge deformation front (Figure 4c). At this stage a new thrust in the prolayer is formed and a similar surface uplift pattern as the one above, initiates. This spatiotemporal pattern of surface uplift is referred to as a surface uplift wave and reflects the migration in activity on thrusts and is thus intimately linked with the frontal accretion cycle. Discrete accelerations of the height above the singularity (Figure 3) prior to the formation of a new thrust within the prolayer support the notion of surface uplift waves.

[24] Finally, the spatiotemporal distribution of ISU mirrors the four stages of bivergent wedge evolution. During stage I ISU is symmetrically distributed above the singularity, while during stage II the location of maximum ISU shifts toward the lower plate, resulting in a topographic asymmetry. This asymmetry is further magnified during stage III, since maximum ISU is associated with the initiation and formation of thrust imbricates within the prowedge. The onset of frontal accretion within the retrowedge (stage IV) marks the transition to a more symmetric wedge topography.

3.3. Strain Accumulation and Propagation

[25] On the basis of the finite strain image and the evolution of deformation map (EDM), the main structural elements such as the initial pop-up, the retroshear zone, individual thrust imbricates within the prowedge and the retrowedge as well as subtle features like back thrusts, footwall shortcuts and out-of-sequence reactivation of thrust imbricates, can be identified (Figures 5a and 5b). The four stages in bivergent wedge evolution proposed above, are also evident from Figure 5b. Stage II is distinguishable from

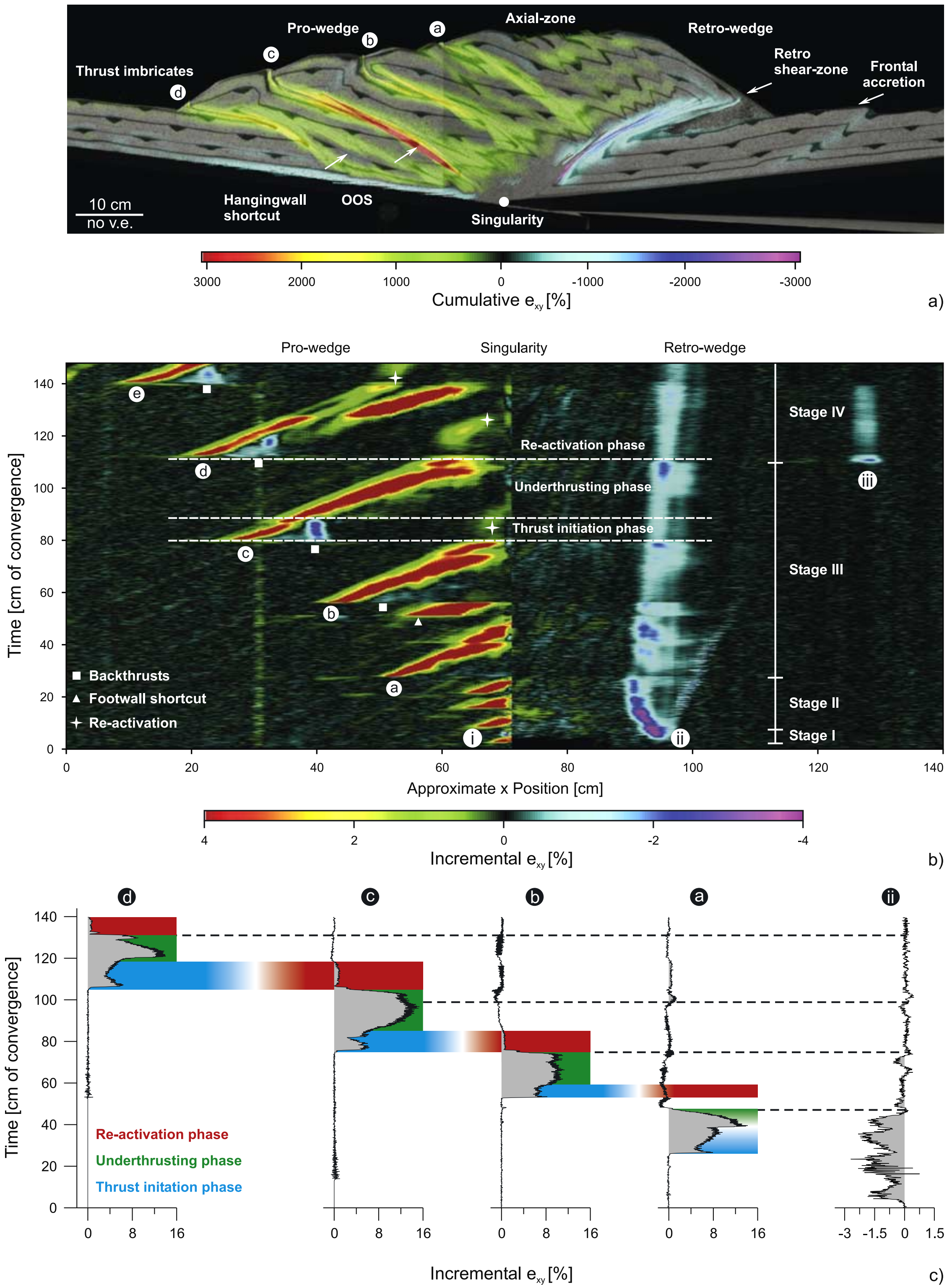

Figure 5

stage I, since the life span of the three narrowly spaced thrusts is significantly longer than the life span of the fore thrust bounding the initial pop-up. In turn, the flat-topped box anticlines of stage III show an even longer life span than the three fore thrusts of stage II, thus allowing for differentiation between these stages. During stage III incremental strain along the retroshear zone decreases markedly, but shows pulses, which predate the formation of a new thrust within the prolayer. These strain pulses are consistent with the surface uplift waves (Figure 4c) and the discrete accelerations of the height above the singularity prior to the formation of a new thrust imbricate within the prolayer (Figure 3) as described above. The onset of stage IV is marked by the emergence of frontal accretion within the retrowedge. During stage IV reactivated thrusts accumulate more and the retroshear zone less, incremental strain, while the latter still shows incremental strain pulses.

3.4. Frontal Accretion Cycle

[26] Further analysis of the EDM in conjunction with the spatiotemporal evolution of the vertical (v_y) and the horizontal (v_x) components of the velocity field (Figure 6) revealed a regular, incremental e_{xy} pattern, which is referred to as the frontal accretion cycle (Figure 6). We propose that each cycle consists of a thrust initiation phase, which in turn is divided into three subphases; an underthrusting phase and a reactivation phase. The latter is coeval with the thrust initiation phase of the following frontal accretion cycle. The nomenclature of the first two phases follows *Hoffmann-Rothe et al.* [2004], whereas the term reactivation phase is introduced in this study.

[27] During the first subphase of the thrust initiation phase, deformation propagates outward along the basal detachment and finally steps up to form a symmetric pop-up. This pop-up evokes a significant decrease of v_x within the prolayer (Figure 6b).

[28] During the second subphase the basal detachment and the fore thrust of the pop-up form a continuous shear zone with a ramp flat geometry. At the same time, the back thrust associated with the pop-up and the previous deformation front cease in activity (Figure 6c).

[29] In the third subphase of the thrust initiation phase, the initial pop-up evolves into a flat-topped box anticline, which is associated with the reactivation of the respective back thrust. Convergence is now taken up by the newly formed fore thrust, its back thrust, the previous fore thrust and the retroshear zone (Figure 6d). In contrast to the first subphase, no significant change in the velocity field occurs during the latter two subphases.

[30] In the following underthrusting phase, both the back thrust and the previous deformation front are abandoned, and the prolayer is considerably overthrust by the prowedge. Convergence is thus taken up by two conjugate shear zones, defining a wedge-scale, symmetric pop-up (Figure 6e). Thus the frontally accreted material is continuously transferred toward the axial zone, rotated back and finally passively uplifted in the hanging wall of the retroshear zone. The associated vertical component of the velocity field is at its maximum within the axial zone and decreases toward the prowedge and the retrowedge (Figures 6a and 6e). Hence the location of maximum v_y has moved from the flat-topped box anticline at the toe of the prowedge toward the axial zone. This observation is in concert with the ISU wave documented earlier (Figure 4).

[31] The underthrusting phase is terminated by thrust initiation phase for the next frontal accretion cycle. During the second subphase of this thrust initiation phase, incremental e_{xy} ceases to accumulate along the previous deformation front, but is reactivated during the respective third subphase (Figure 6f). The previous deformation front remains active until the next underthrusting phase commences. Finally, note that the spatiotemporal distribution of v_y, not v_x, is indicative of the currently active phase within a frontal accretion cycle.

[32] The evolution of incremental e_{xy} at points located within individual ramp segments of the fore thrusts shows one absolute and two local maxima, which are linked with the three phases of the frontal accretion cycle identified above (Figure 5c). The two local maxima correspond to the thrust initiation phase and the reactivation phase respectively, with the former attaining higher magnitudes than the latter. The absolute maximum of e_{xy} is linked with the underthrusting phase. Together, these observations suggest that each phase within a frontal accretion cycle is associated with different magnitudes and rates of strain accumulation. This can be also recognized in Figure 7, which shows the evolution of the cumulative displacement for each thrust imbricate.

[33] The strain history of the retroshear zone follows an oscillating pattern, whereby e_{xy} maxima predate the formation of a new thrust imbricate within the prolayer (Figure 5c). This is consistent with the information deduced from the EDM (Figure 5b). The decreasing amplitude of these maxima with ongoing convergence indicates that the ability

Figure 5. (a) Distribution of finite e_{xy}, i.e., after 140 cm of convergence for the reference experiment. Labels a to d denote thrusts within the prowedge. White arrows point to main out-of-sequence thrust, a hanging wall shortcut, the retroshear zone, and the frontal accretion within the retrowedge. (b) Evolution of deformation map (EDM) for the reference experiment. Letters in circles refer to fore thrusts within the prowedge (see Figure 2g). Roman i denotes proshear of initial pop-up, ii denotes the respective retroshear, and iii denotes frontal accretion within the retrowedge. Four stages of bivergent wedge evolution as well as phases of accretion cycle are explained graphically. Note the pulsating e_{xy} accumulation of the retroshear zone ii. (c) Incremental e_{xy} accumulation of fore thrusts (a to d) and the retroshear zone ii through time. The three phases of the frontal accretion cycle are color coded to visualize strain transfer. We highlight that each phase shows different incremental e_{xy} magnitudes. On the basis of the reference and the other three experiments (Figure S5), we found that the underthrusting phase takes up ∼50% of the duration of a frontal accretion cycle. Both the thrust initiation and the reactivation phase take up ∼25% equally. See the auxiliary material for derivation of both figures.

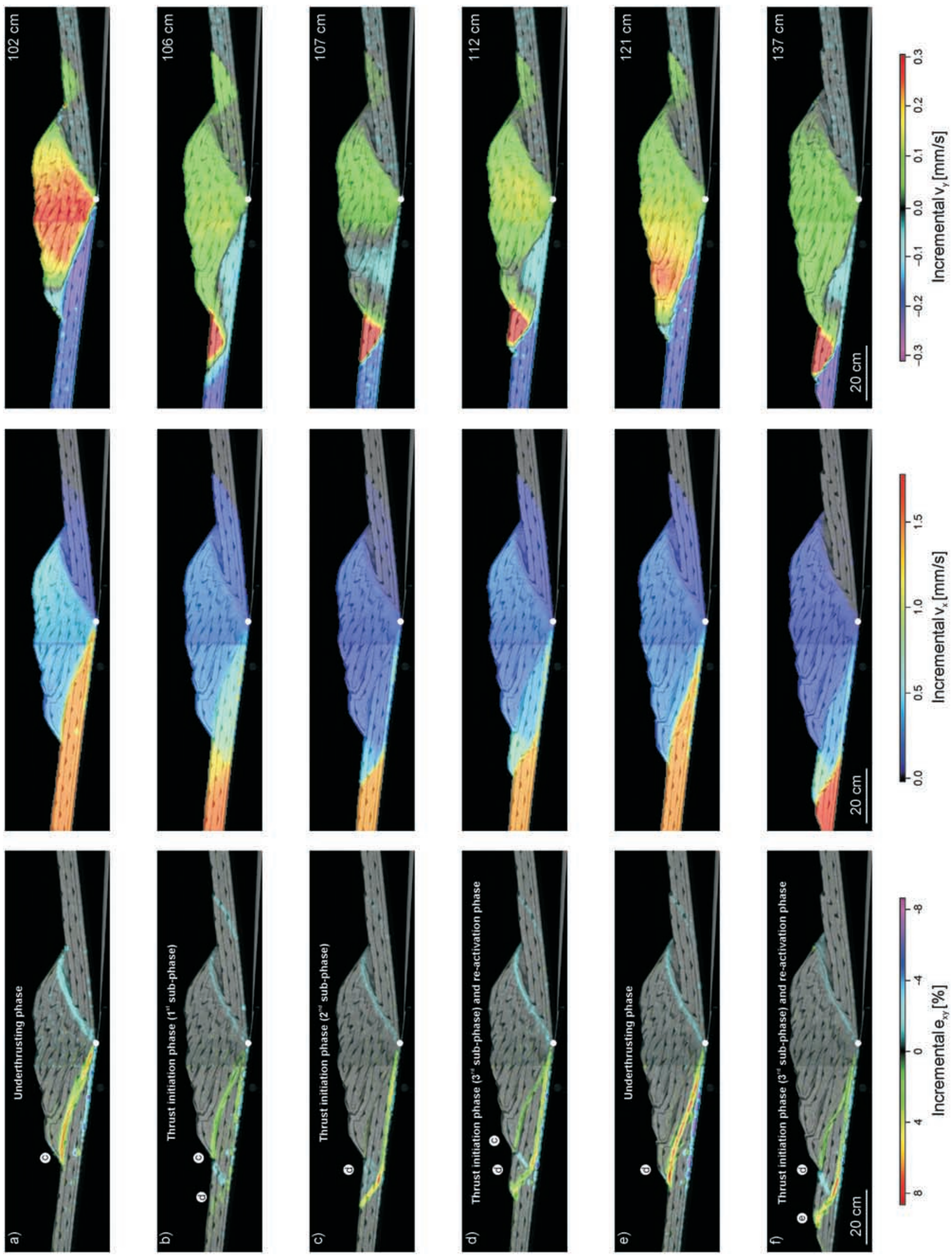

a)
Underthrusting phase
b)
Thrust initiation phase (1st sub-phase)
c)
Thrust initiation phase (2nd sub-phase)
d)
Thrust initiation phase (3rd sub-phase) and re-activation phase
e)
Underthrusting phase
f)
Thrust initiation phase (3rd sub-phase) and re-activation phase
102 cm
106 cm
107 cm
112 cm
121 cm
137 cm
20 cm
Incremental e_{xy} [%]
Incremental v_x [mm/s]
Incremental v_y [mm/s]

Figure 6

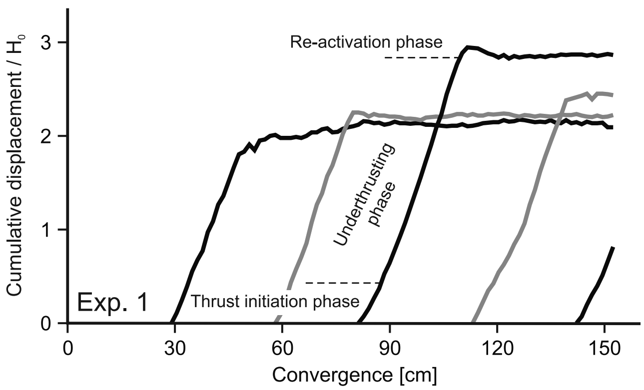

Figure 7. Cumulative thrust displacements for each thrust within the prowedge of the reference experiment 1. Data were taken at every 0.75 cm of convergence. Alternation of black and grey curves is to aid visualization. Displacement accumulation gradient varies through time and can be correlated with the three phases of the frontal accretion cycle.

to transfer strain between the fore thrusts and the retroshear zone decreases with increasing distance between them.

4. Toward the Concept of a Frontal Accretion Cycle

[34] Confidence about the appropriateness of the selected setup is derived from the observation that all conducted experiments followed a similar evolutionary pathway, as proposed by other sandbox and numerical simulations [*Malavieille*, 1984; *Brown et al.*, 1993; *Willett et al.*, 1993; *Beaumont et al.*, 1996; *Wang and Davis*, 1996; *Beaumont et al.*, 2000; *Storti et al.*, 2000; *Del Castello et al.*, 2004; *McClay and Whitehouse*, 2004; *Naylor et al.*, 2005; *Hoth et al.*, 2006]. This suggests also reproducibility despite different setups and methodological approaches. The proposed model evolution is also consistent with results from balanced cross sections from the European Alps [*Pfiffner et al.*, 2000], the Pyrenees [*Beaumont et al.*, 2000] and the German Variscides [*Schäfer et al.*, 2000], and has been more thoroughly discussed by *Hoth et al.* [2006].

4.1. Conceptual Model

[35] Although we found that bivergent wedge evolution is very similar despite different mechanical stratigraphies, a high degree of similarity with respect to the spatiotemporal distribution of strain was not expected, but was observed. Indeed our experimental results indicate that the frontal accretion cycle with its three phases is very robust with respect to the parameters tested (Figure S5 in the auxiliary material). We therefore propose the conceptual model of a frontal accretion cycle (Figure 8a), which can be viewed as an extension of the one postulated by *Gutscher et al.* [1998] and used by *Hoffmann-Rothe et al.* [2004]. Accordingly, a frontal accretion cycle in its simplest form might evolve as follows:

[36] During the first phase, i.e., the thrust initiation phase, convergence is taken up by four thrust faults: the fore thrust, which defines the deformation front; the associated back thrust; an internal thrust, i.e., the previous deformation front, and the retroshear zone. The resultant incremental surface uplift is highest above the ramp segment of the fore thrust and lowest above the retroshear zone.

[37] In the underthrusting phase that follows the fore thrust evolves from a ramp flat, via a ramp toward a flat ramp geometry. The latter geometry is therefore similar to the one of the retroshear zone (Figure 6). Hence the asymmetry associated with the thrust initiation phase is abandoned in favor of a more symmetric geometry during the late stages of the underthrusting phase, with the result that the entire sand wedge shortens horizontally and grows vertically. At the same time, a surface uplift wave, which mirrors locations of high e_{xy} accumulation, migrates through the entire wedge until it reaches the retroshear zone.

[38] During the third phase, i.e., the reactivation phase, deformation propagates outward into the prolayer to form a new flat-topped box anticline and a new frontal accretion cycle commences. The fore thrust under consideration is now located in the hanging wall of the newly formed fore thrust. This implies that the third phase of a frontal accretion cycle is coeval with the first phase of the following cycle. Therefore strain transfer between two successive fore thrusts cannot be considered as abrupt; that is, one thrust is "switched" off, while the other is switched on. Instead, strain is transferred gradually; that is, the decay in activity of a fore thrust is simultaneous with the increasing activity of the newly formed one (Figures 5c and S5). It follows that incremental e_{xy} is not only partitioned in space but also in time. The magnitude of e_{xy} taken up by each thrust depends on its relative strength, which changes predictably through time, as outlined below (Figure 8b).

[39] Results from ring shear measurements and triaxial compression tests indicate that the initiation of a thrust is associated with the successive formation and growth of isolated precursor structures, i.e., small-scaled shear zones [*Mandl et al.*, 1977; *Mandl*, 1988; *Okubo and Schultz*, 2005]. At the same time individual grains are pressed more firmly together, which increases the frictional resistance of the sand to the imposed shear stress: strain hardening [*Mandl*, 1988]. The resultant strain accumulation is low. As shearing continuous beyond this state the shear stress has to rise and may finally reach the yield criterion, leading to the coalescence of these small-scaled shear zones [*Mandl et al.*, 1977; *Mandl*, 1988; *Marone*, 1998]. Further shear induces a rearrangement of grains, which are now more

Figure 6. Sequential development of an accretion cycle. Left to right show incremental e_{xy} and the respective horizontal and vertical component of the velocity field. The term incremental describes the time between two successive PIV images. Numbers on the right indicate cm of convergence. Interpretation of the e_{xy} pattern in terms of the accretion cycle is given as well. Note that the location of maximum v_y during subsequent underthrusting phases is systematically shifted from the axial zone during early frontal accretion cycles toward the center of the prowedge during later frontal accretion cycles.

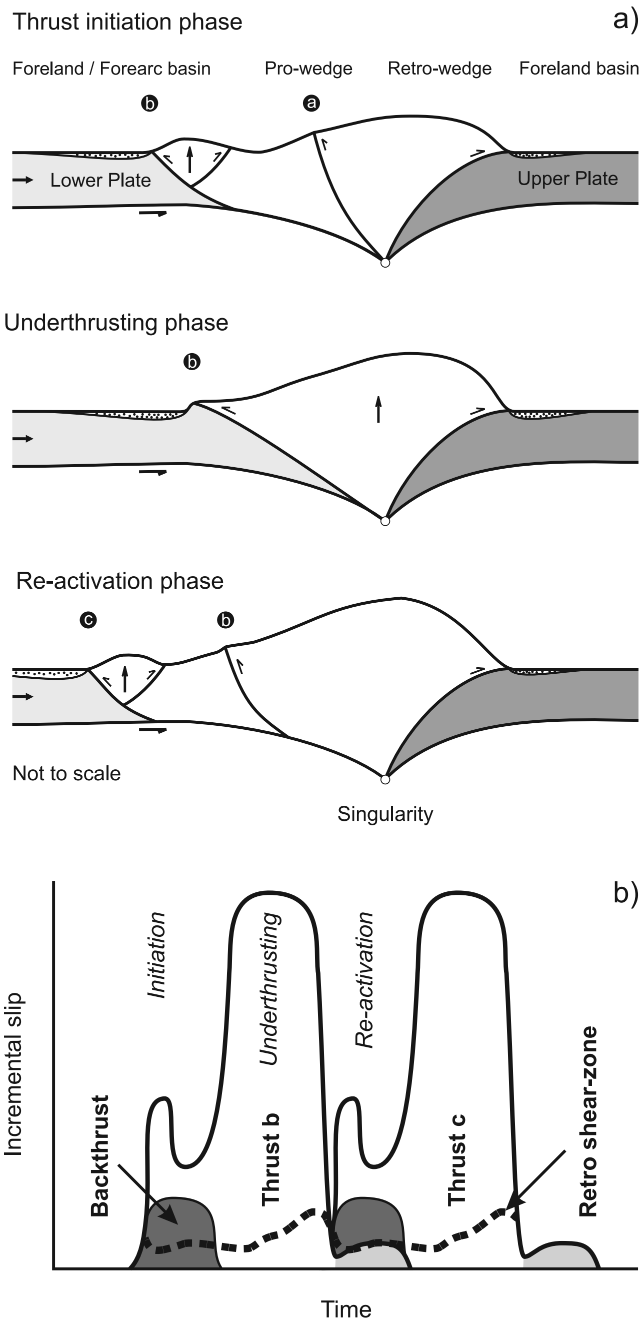

Figure 8. (a) Conceptual model of a frontal accretion cycle with its three phases, i.e., thrust initiation, underthrusting, and reactivation phases. Locations of maximum incremental surface uplift are indicated with an arrow. The accretion cycle is associated with a strain and a surface uplift wave. Both are initiated at the toe of the prowedge and migrate through the entire bivergent wedge until the retroshear zone is reached. The phase within an accretion cycle controls thus the timing, location, and magnitude of deformation (e_{xy}) and surface uplift. (b) Incremental e_{xy} (slip) accumulation for all thrust, which are active during two accretion cycles. Magnitudes were taken from experiment 1. Phase within accretion cycle determines thus the location and magnitude of strain and slip accumulation. Therefore strain and slip are partitioned in time and space.

preferentially orientated with respect to the shear direction: strain softening [*Mandl*, 1988]. The resultant strain accumulation is high.

[40] On the basis of the evolution of strain accumulation for each thrust as derived from PIV analysis (Figure 5c), we infer that the three phases of a frontal accretion cycle are controlled by the strain hardening and softening processes associated with the evolution of these shear zones as outlined above. Accordingly, the thrust initiation phase would correspond to the strain hardening, the underthrusting phase to the strain-softening part of the stress-strain evolution. Continuous transfer of the thrust under consideration toward the singularity, in conjunction with an increasing load upon this thrust, leads to its final locking during the reactivation phase. The respective incremental e_{xy} magnitudes are low. Given that incremental e_{xy} accumulation along the retroshear zone mirrors this evolution (Figure 5c), we postulate that the entire bivergent wedge is subjected to a strain-hardening/strain-softening cycle. Thus, during the thrust initiation phase the wedge is strain softest but with continued convergence successively strengthened. At the very final stage of the underthrusting phase, the wedge is assumed to be "strain hardest." Although brittle failure by itself is strain rate-independent [*Byerlee*, 1978], the ability of sand to exhibit strain hardening and softening introduces a temporal dependence on the magnitude of strain, accumulated on each individual thrust during a certain time interval. The frontal accretion cycle is therefore considered as an internal clock of wedge-scaled deformation and surface uplift. Differences between experiments in the duration and magnitude of individual phases relate either to the depth to the detachment or to the strength of the prowedge (see section 4.3).

[41] The cumulative displacement evolution of thrusts reflects the three phases of the frontal accretion cycle. Therefore the former can be used to constrain the latter, if strain monitoring techniques, such as PIV, are not available (Figure 7). Thus the conceptual model of a frontal accretion cycle is able to integrate and to explain previously unrelated observations such as (1) the periodicity of thrusting [*Cadell*, 1888; *Mulugeta and Koyi*, 1992; *Gutscher et al.*, 1998], (2) the topographic evolution of sand wedges, especially the significant increase of the vertical growth rate at the rear of a wedge prior to the formation of a new thrust within the prolayer [*Koyi*, 1995; *Gutscher et al.*, 1998; *Storti et al.*, 2000; *Naylor et al.*, 2005], (3) the cumulative displacement evolution of thrusts [*Koyi*, 1995; *Storti et al.*, 2000; *Del Castello et al.*, 2004; *McClay and Whitehouse*, 2004] and (4) the occurrence of different thrust sequences, i.e. forward breaking, synchronous and out-of-sequence thrusting [*Storti et al.*, 2000]. The latter would only be transient phenomena within the evolution of an accretion cycle. "Local" factors such as crustal inheritance, surface processes or changes of the mechanical stratigraphy need not to be invoked to explain changes in thrust activation. Previous experiments incorporating erosion [*Hoth*, 2006, available at http://www.gfz-potsdam.de/bib/pub/str0606/0606.htm] support this assertion.

4.2. Evidence From Field Studies

[42] On the basis of structural work along the Chelungpu thrust (Taiwan) and analytical considerations, *Heermance*

and Evans [2006] demonstrated that the geometry of the hanging wall block controls the magnitude of the force resisting slip. The latter is lower for hanging wall blocks with a wedge geometry than for those with a ramp flat geometry. This is consistent with the observation that during the underthrusting phase with its wedge-shaped hanging wall block, e_{xy} magnitudes are highest (Figure 5c). Microstructural work in the Appalachian fold and thrust belt led *Wojtal and Mitra* [1986] to conclude that the emplacement of a thrust sheet takes place at least in two stages: The first is associated with strain hardening; the second is associated with strain softening. Similarly, *Travé et al.* [2000] reported two microfracture stages in the El Guix anticline (Pyrenees). During the first stage, a network of discontinuous microfractures developed, which allowed only local meteoric fluids to circulate. In the second stage, a continuous thrust fault formed, providing a regional fluid conduit [*Travé et al.*, 2000]. Using the terminology of this study, the first and the second stage of *Wojtal and Mitra* [1986] and *Travé et al.* [2000] can be linked to the thrust initiation and to the underthrusting phase, respectively. *Meigs et al.* [1996] reconstructed the displacement evolution of the South Pyrenean Sierras Marginales thrust, which is very similar to the displacement histories observed during own experiments (Figure 9). They further proposed that the displacement transfer from more internal to more external thrusts is a continuous process, rather than a stepwise sequence of formation, displacement, and deactivation of thrusts. This conclusion agrees well with the results of the experiments presented here. A similar observation was made by *Butler and Bowler* [1995] in the Chartreuse district of the French Subalpine thrust belt. They concluded that thrusts evolve through a displacement rate cycle, which is concordant with the accretion cycle we observe. *Jones et al.* [2004] investigated the evolution of the Catalan fold and thrust belt. On the basis of balanced cross sections they proposed a thrust sequence, similar to the one observed in this study.

[43] A similar nonlinear topographic growth above a ramp segment as recognized during the experiments, has been reported from a late Quaternary anticline in New Zealand [*Jackson et al.*, 2002] and in numerical simulations [*Bernal et al.*, 2004]. Additionally, *Masaferro et al.* [2002] concluded that the Neogene-Quaternary growth of the Santaren anticline (Cuban fold and thrust belt) was characterized by several tectonic uplift pulses of different duration

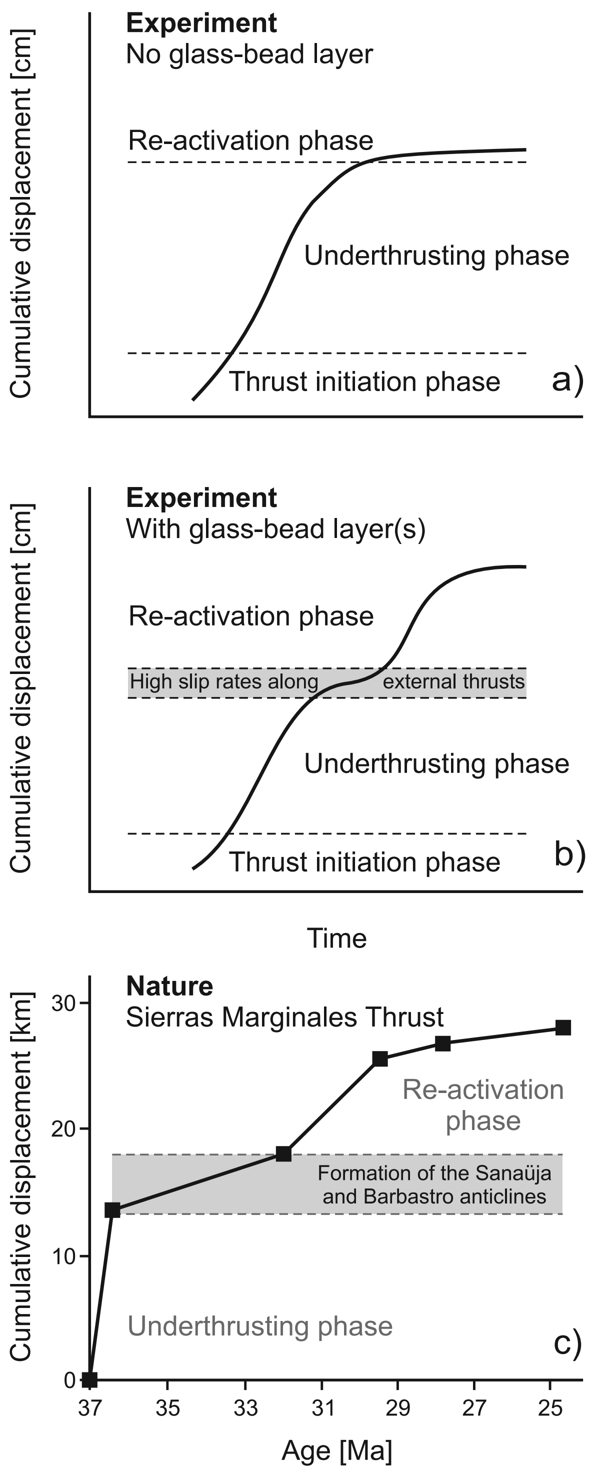

Figure 9. Generalized cumulative displacement evolution as derived from experiential results. Please see the auxiliary material for details. Displacement evolution (a) without and (b) with temporal offset between the underthrusting and the reactivation phase (gray area). During this time period more external thrusts, i.e., thrusts located within the very frontal part of the prowedge, show high slip rates or a new thrust is formed within the incoming layer. Dashed lines in Figures 9a and 9b mark phase boundaries. (c) Cumulative displacement of the Sierras Marginales Thrust, southern Pyrenees, which detaches within Triassic Keuper evaporites. Solid squares indicate data points (modified after *Meigs et al.* [1996]). Tentative interpretation in terms of the conceptual model of cyclic frontal accretion is provided. Grey area (36.5–32 Ma) corresponds to increase of slip rates along the base (evaporites) of the foreland basin succession, which was associated with the formation of the Sanaüja and the Barbastro anticlines [*Meigs et al.*, 1996]. Both anticlines are located in the footwall of the Sierras Marginales Thrust. These observations are thus similar to the ones derived from experiments with an internal glass bead layer, indicating as well the consistency between model prediction and observations derived from field studies.

Table 2. Summary of Experimentally Derived Results

Observations	Experiment 1	2	3	4
Number of weak layers	0	1	2	0
Frontal accretion in retrowedge	yes	yes	no	yes
Number of thrust imbricates in prowedge after 140 cm of convergence	5	8	8	5
Sample standard deviation of wavelength of frontal accretion[a] s_{fw}	0.13	0.30	0.15	0.19
Sample standard deviation of spacing of frontal accretion[a] s_{fs}	0.15	0.09	0.07	0.15
Sample standard deviation of wavelength of basal accretion s_{bw}		0.47	0.90	
Out-of-sequence displacement index (OOSD)	0.62	8.1	3.73	3.95

[a]Without footwall shortcuts.

and intensity, interrupted by periods of variable duration in which no fold growth occurred.

4.3. Timing of Thrust Initiation

[44] In section 4.2 the frontal accretion cycle was considered as an internal clock, which controls the activation, reactivation and deactivation of thrusts. The sample standard deviation of the wavelength of frontal accretion s_{fw} provides a measure of the temporal regularity of the initiation of fore thrusts within the prolayer (Table 2).

[45] A constant timing, i.e., a low s_{fw} value indicates that the wedge response to accretion by internal deformation is the same for every frontal accretion cycle. High s_{fw} values suggest that this response varies with each frontal accretion cycle and that the timing between two thrust initiation events varies as well. In terms of the minimum work theory this means that internal deformation is favored until the initiation of a new thrust within the prolayer would require less work [e.g., *Gutscher et al.*, 1998]. Both the introduction of weak layers (this study) and the simulation of prowedge erosion [*Hoth et al.*, 2006] reduce the strength of the prowedge with respect to the retrowedge, leading to prolonged internal deformation in favor of the propagation of deformation into the foreland, and thus to higher s_{fw} values. This is also evident from the EDM (Figure S5). It follows that high magnitudes of internal deformation evoke longer durations of the frontal accretion cycle.

[46] These observations indicate that for a given convergence velocity, the minimum time required for a frontal accretion cycle is proportional to the length of the frontally accreted imbricate. Also, the aspect ratio (length:depth-to-detachment) of the experimentally generated thrust imbricates (Figure 3), which mimics the ratio between basal and internal friction, is ~3 to 1 [*Platt*, 1988; *Gutscher et al.*, 1996; *Oncken et al.*, 2000]. This is the same ratio as the one found in fold and thrust belts [*Oncken et al.*, 2000], lending additional support for the correct scaling of the mechanics of sand wedges. Combining the above observations, we propose that the minimum duration of a thrust initiation and its associated underthrusting phase can be calculated as follows:

$$t = 3D/v, \tag{1}$$

where t is the duration (years), D is the depth to the detachment (m) and v is the convergence velocity (m/yr). Since the reactivation phase takes up ~25% of the entire duration of a frontal accretion cycle (Figures 5 and S5), equation (1) changes to $t_c = 4D/v$, where t_c is the complete duration of a frontal accretion cycle. Equation (1) was tested with respect to the Alaskan accretionary wedge (EDGE Profile [*Moore et al.*, 1991]). Using biostratigraphic and geometric constraints, *von Huene et al.* [1998] calculated the time span of deformation within segment II [*von Huene et al.*, 1998, Figure 4] to be 0.22–0.24 Ma, which agrees well with an estimation of 0.22 Ma derived from equation (1).

[47] On the basis of equation (1), we found that the duration of frontal accretion cycles in the majority of active accretionary wedges is on the order of 10^4–10^5 years (Figure 10), a similar time span as climatic cycles [*Zachos et al.*, 2001]. In order to unequivocally determine whether an observation such as surface uplift, exhumation, erosion or sedimentation results from tectonic or climatic cyclicity, regional studies that cover at least the prowedge and the axial zone are needed. Given the proposed time span of frontal accretion cycles with their three phases, high resolution time series are required. We suggest that the temporal resolution of theses time series should be on the order of 1/4 of the expected duration of a frontal accretion cycle. Given that the transition between two successive phases within experimental frontal accretion cycles is abrupt, we speculate that such a transition may occur at a timescale of ~10^2 *to* 10^3 years.

4.4. Implications for Natural Bivergent Wedges

[48] Given the good agreement with previous work [*Gutscher et al.*, 1998; *Storti et al.*, 2000; *Del Castello et al.*, 2004; *Hoffmann-Rothe et al.*, 2004; *Hoth et al.*, 2006] and the scale invariance of brittle behavior, we propose that our results are applicable to bivergent orogens, to fold and thrust belts and to accretionary prisms. Accordingly, the implications derived from the experiments are confined to no specific spatial and temporal scale and may be tested in all three settings. However, some caution must be taken when applying our results to bivergent orogens, since we focus only on lower temperature orogens, where brittle behavior prevails. High exhumation rates in natural orogens may lead to the removal of the highest strength part of the continental crust, which significantly reduces its integral strength. At this stage ductile, temperature- and time-dependent processes might dominate [*Zeitler et al.*, 2001; *Koons et al.*, 2002]. We also restrict our implications to those settings with one major detachment. If several detachments operate at the same time, the expected signal either in deformation or surface uplift may be difficult to detect. Nevertheless, the proposed conceptual model of a frontal accretion cycle bears some important implications.

[49] 1. The transience of deformation is the rule and not the exception. This would be one explanation for the commonly observed discrepancy between geodetic, paleoseismologic and geologic estimates of fault slip [*Coutand et al.*, 2002; *Hubert-Ferrari et al.*, 2005]. Thus interpolation of slip rates from different temporal scales and resultant predictions of recurrence intervals of earthquakes within bivergent wedges can only be successful if the phase within

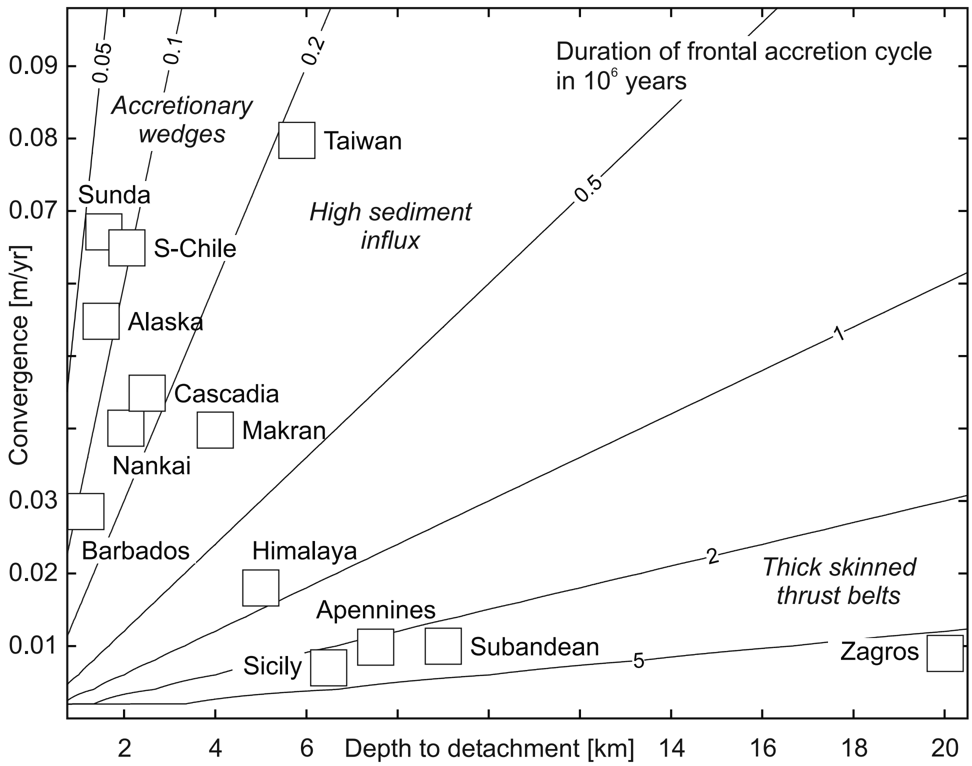

Figure 10. Minimum duration of the first two phases within a frontal accretion cycle. Diagram is calculated from equation (1). Data from natural examples are based on GPS velocities and seismic sections or balanced profiles. Variabilities with respect to along- and across-strike changes of *d* and *v* are not taken into account. Three domains can be distinguished: (1) thick-skinned thrust belts, (2) bivergent wedges with high sediment influx, and (3) accretionary wedges. Note that most of the frontal accretion cycles within accretionary wedges have a duration of $\sim 10^5$ years. Data are taken from Alaska [*Fruehn et al.*, 1999]; Apennines [*Oldow et al.*, 2002; *Tozer et al.*, 2002]; Barbados [*DiLeonardo et al.*, 2002]; Cascadia [*Khazaradze et al.*, 1999; *Adam et al.*, 2004]; Chile, ENAP line 732, 39° *S* [*Díaz-Naveas*, 1999; *Norabuena et al.*, 1999]; Himalayan Foothills (MFT) [*Bilham et al.*, 1997; *Lavé and Avouac*, 2000]; Makran [*DeMets et al.*, 1990; *Kopp et al.*, 2000]; Nankai [*Seno et al.*, 1993; *Moore et al.*, 2001]; Sicily [*Adam*, 1996]; Subandes (NW Argentina) [*Echavarria et al.*, 2003]; Sunda Arc [*Prawirodirdjo et al.*, 2000; *Kopp and Kukowski*, 2003]; Taiwan, Chelungpu Thrust [*Yu et al.*, 1997; *Yue et al.*, 2005]; Zagros, Mountain Front Fault [*Vernant et al.*, 2004; *Molinaro et al.*, 2005].

the frontal accretion cycle is identified. Also, in-sequence, synchronous and out-of-sequence thrusting are considered as kinematic stages within a frontal accretion cycle.

[50] 2. Along-strike variations of thrust seismicity result from a thrust that is not in the same phase of the accretion cycle along strike. Such along-strike changes should be taken into account when seismic hazard potential is evaluated. Changes in the plate kinematics, the climate/erosion scheme or of other local factors need not be invoked to explain the spatiotemporal variability of strain accumulation.

[51] 3. The geometry of the deformation front may be used to infer the seismic and/or landslide hazard potential, since the geometry is indicative of the active phase within the frontal accretion cycle.

[52] 4. Spatial and temporal offset of cause and response. The initiation of a new thrust within the prolayer (cause) is temporally offset from the resulting "strain pulse" at the retroshear zone (response). However, the magnitude of strain transfer between the prowedge and the retrowedge decreases, while the prowedge grows laterally. During subsequent stages of bivergent wedge evolution this strain transfer may not be detectable.

[53] 5. Time dependence of incremental slip along thrusts implies that the source and availability of fluids/hydrocarbons may vary during a frontal accretion cycle. The migration of fluids is probably highest during the underthrusting phase.

[54] 6. A surface uplift wave reflects migrating activity on thrusts and hence mirrors an accretion cycle. In contrast, the horizontal component of the velocity field is not indicative of the active phase within a frontal accretion cycle. During such a cycle, surface uplift decreases with increasing distance from the deformation front, but may reach up to 1/2 of the thickness of the incoming layer at the axial zone. Successive relief rejuvenation of more internal parts of a bivergent wedge may lead to the successive unroofing and erosion of hinterland lithologies and finally to provenance cycles in synkinematic basins (Figure 8a). Since basal accretion episodes have not evoked a detectable trace within

the ISU during experiments, we speculate that this might be similar in nature, if the bivergent wedge grows dominantly by frontal accretion.

[55] 7. A self-similar growth assumption for thrust induced topography should be invoked with care.

5. Conclusions

[56] Bivergent wedges are found to operate at several spatial scales, ranging from accretionary prisms to entire orogens. On the basis of 2-D scaled sandbox simulations we have developed a conceptual model of cyclic frontal accretion within bivergent wedges. Each cycle consists of a thrust initiation, an underthrusting and a reactivation phase, which control the location and magnitude of deformation within and surface uplift of a bivergent wedge. Consequently, the frontal accretion cycle is considered as an internal clock of bivergent wedge deformation and surface uplift. Thus the former can be used to constrain the latter or vice versa.

[57] The proposed conceptual model provides an explanation for the commonly observed transient behavior of deformation and surface uplift and links the long-term evolution of bivergent wedges with the short-term variability of slip accumulation. This variability can be explained without the need to invoke changes in the far-field plate kinematics or in the climate/erosion regime.

[58] Strain transfer between thrusts within the prowedge is a gradual process. Incremental strain accumulation at the retroshear follows an oscillating pattern, which mirrors the phases within the frontal accretion cycle.

[59] Finally, we propose that the geometry of the deformation front can be used to constrain the phase within a frontal accretion cycle, which in turn has implications for seismic and landslide hazard assessment studies.

[60] **Acknowledgments.** We are grateful to Onno Oncken, Anke Friedrich, and Dirk Scherler for encouraging discussion. Helpful suggestions by Rupert Sutherland (Associate Editor) and critical comments by Phaedra Upton, Guy Simpson, and an anonymous reviewer are thankfully acknowledged. Alan Levander kindly improved the English. All experiments were carried out in the Geodynamics Laboratory of the GeoForschungsZentrum Potsdam, Germany. Günther Tauscher built the experimental setup. Funding to S.H. was kindly provided by Deutsche Forschungsgemeinschaft (DFG Leibniz-Program On7/10-1), SonderForschungsBereich 267 project F1, and the Center for System Analysis of Geoprocesses.

References

Adam, J. (1996), Kinematik und Dynamik des neogenen Falten- und Deckengürtels in Sizilien, *Berliner Geowiss. Abh. A*, *185*, 171 pp.

Adam, J., D. Klaeschen, N. Kukowski, and E. Flueh (2004), Upward delamination of Cascadia Basin sediment infill with landward frontal accretion thrusting caused by rapid glacial age material flux, *Tectonics*, *23*, TC3009, doi:10.1029/2002TC001475.

Adam, J., J. Urai, B. Wieneke, O. Oncken, K. Pfeiffer, N. Kukowski, J. Lohrmann, S. Hoth, W. van der Zee, and J. Schmatz (2005), Shear localisation and strain distribution during tectonic faulting: New insights from granular-flow experiments and high-resolution optical image correlation techniques, *J. Struct. Geol.*, *27*(2), 283–301, doi:10.1016/j.jsg.2004.08.008.

Beaumont, C., P. Fullsack, and J. Hamilton (1994), Styles of crustal deformation in compressional orogens caused by subduction of the underlying lithosphere, *Tectonophysics*, *232*(1–4), 119–132.

Beaumont, C., S. Ellis, J. Hamilton, and P. Fullsack (1996), Mechanical model for subduction-collision tectonics of alpine-type compressional orogens, *Geology*, *24*, 675–678.

Beaumont, C., J. A. Munoz, J. Hamilton, and P. Fullsack (2000), Factors controlling the alpine evolution of the central Pyrenees inferred from a comparison of observations and geodynamical models, *J. Geophys. Res.*, *105*, 8121–8145.

Bernal, A., S. Hardy, R. Gawthorpe, and E. Finch (2004), Stratigraphic expression of the lateral propagation and growth of isolated fault-related uplifts, *Basin Res.*, *16*(2), 219–233.

Bilham, R., et al. (1997), GPS measurements of present-day convergence across the nepal himalaya, *Nature*, *386*(6620), 61–64.

Bombolakis, E. G. (1986), Thrust-fault mechanics and origin of a frontal ramp, *J. Struct. Geol.*, *8*(3–4), 281–290.

Boyer, S. E. (1992), Geometric evidence for synchronous thrusting in the southern Aberta and northwest Montana thrust belts, in *Thrust Tectonics*, edited by K. R. McClay, pp. 377–390, CRC Press, Boca Raton, Fla.

Boyer, S. E. (1995), Sedimentary basin taper as a factor controlling the geometry and advance of thrust belts, *Am. Sci.*, *295*(10), 1220–1254.

Boyer, S. E., and D. Elliott (1982), Thrust systems, *AAPG Bull*, *66*(9), 1196–1230.

Brown, R., C. Beaumont, and S. Willett (1993), Comparison of the Selkirk fan structure with mechanical models: Implications for interpretation of the southern Canadian Cordillera, *Geology*, *21*, 1015–1018.

Butler, R. W. H. (1987), Thrust sequences, *J. Geol. Soc. London*, *144*(4), 619–634.

Butler, R. W. H. (2004), The nature of "roof thrusts" in the Moine thrust belt, northwest Scotland: Implications for the structural evolution of thrust belts, *J. Geol. Soc. London*, *161*(5), 849–859.

Butler, R. W. H., and S. Bowler (1995), Local displacement rate cycles in the life of a fold-thrust belt, *Terra Nova*, *7*(4), 408–416.

Byerlee, J. (1978), Friction of rocks, *Pure Appl. geophys.*, *116*(4–5), 615–626.

Cadell, H. M. (1888), Experimental researches in mountain building, *Trans. R. Soc. Edinburgh.*, *35*.

Choukroune, P. (1989), The ECORS Pyrenean deep seismic profile reflection data and the overall structure of an orogenic belt, *Tectonics*, *8*(1), 23–39.

Coutand, I., M. R. Strecker, J. R. Arrowsmith, G. Hilley, R. C. Thiede, A. Korjenkov, and M. Omuraliev (2002), Late Cenozoic tectonic development of the intramontane Alai Valley, (Pamir-Tien Shan region, central Asia): An example of intracontinental deformation due to the Indo-Eurasia collision, *Tectonics*, *21*(6), 1053, doi:10.1029/2002TC001358.

Cristallini, E. O., A. H. Cominguez, V. A. Ramos, and E. Mercerat (2004), Basement double-wedge thrusting in the northern Sierras Pampeanas of Argentina (27°S): Constraints from deep seismic reflection, in *Thrust Tectonics and Hydrocarbon Systems*, edited by K. R. McClay, *AAPG Mem.*, *82*, 65–90.

Dahlen, F. A. (1990), Critical taper model of fold-and-thrust belts and accretionary wedges, *Annu. Rev. Earth Planet. Sci.*, *88*, 55–99.

Davis, D., J. Suppe, and F. A. Dahlen (1983), Mechanics of fold-and-thrust belts and accretionary wedges, *J. Geophys. Res.*, *88*(2), 1153–1172.

DeCelles, P. G., and K. A. Giles (1996), Foreland basin systems, *Basin Res*, *8*(2), 105–123.

Del Castello, M., G. A. Pini, and K. R. McClay (2004), Effect of unbalanced topography and overloading on Coulomb wedge kinematics: Insights from sandbox modeling, *J. Geophys. Res.*, *109*, B05405, doi:10.1029/2003JB002709.

DeMets, C., R. Gordon, D. Argus, and S. Stein (1990), Current plate motions, *Geophys. J. Int.*, *101*(2), 425–478.

Díaz-Naveas, J. L. (1999), *Sediment subduction and accretion at the Chilean Convergent Margin between 35°S and 40°S*, 129 pp., Univ. of Kiel, Kiel, Germany.

DiLeonardo, C. G., J. C. Moore, S. Nissen, and N. Bangs (2002), Control of internal structure and fluid-migration pathways within the Barbados Ridge décollement zone by strike-slip faulting: Evidence from coherence and three-dimensional seismic amplitude imaging, *Geol. Soc. Am. Bull*, *114*(1), 51–63.

Echavarria, L., R. Hernandez, R. Allmendinger, and J. Reynolds (2003), Subandean thrust and fold belt of northwestern Argentina: Geometry and timing of the Andean evolution, *AAPG Bull.*, *87*(6), 965–985.

Fruehn, J., R. von Huene, and M. Fisher (1999), Accretion in the wake of terrane collision: The Neogene accretionary wedge off Kenai Peninsula, Alaska, *Tectonics*, *18*(2), 263–277.

Gutscher, M. A., N. Kukowski, J. Malavieille, and S. Lallemand (1996), Cyclical behavior of thrust wedges: Insights from high basal friction sandbox experiments, *Geology*, *24*, 135–138.

Gutscher, M. A., N. Kukowski, J. Malavieille, and S. E. Lallemand (1998), Episodic imbricate thrusting and underthrusting; analog experiments and mechanical analysis applied to the Alaskan accretionary wedge, *J. Geophys. Res.*, *103*(5), 10,161–10,176.

Hampel, A., J. Adam, and N. Kukowski (2004), Response of the tectonically erosive south Peruvian forearc to subduction of the Nazca Ridge: Analysis of three-dimensional analogue experiments, *Tectonics*, *23*, TC5003, doi:10.1029/2003TC001585.

Hardy, S., C. Duncan, J. Masek, and D. Brown (1998), Minimum work, fault activity and the growth of critical wwedges in fold and thrust belts, *Basin Res.*, *10*, 365–373.

Heermance, R., and J. Evans (2006), Geometric evolution of the Chelungpu fault, Taiwan: The mechanics of shallow frontal ramps and fault imbrication, *J. Struct. Geol.*, *28*(5), 929–938, doi:10.1016/j.jsg.2006.01.015.

Hoffmann-Rothe, A., N. Kukowski, and O. Oncken (2004), Phase dependent strain partitioning in obliquely convergent settings, in, *Boll. Geofis.*, *45*, 1 supp, 93–97.

Hoth, S. (2006), Deformation, erosion and natural resources in continental collision zones. Insight from scaled sandbox simulations, STR 06/06, 153 pp., GeoForschungsZentrum Potsdam, Potsdam, Germany.

Hoth, S., J. Adam, N. Kukowski, and O. Oncken (2006), Influence of erosion on the kinematics of bivergent orgens. results from scaled sandbox simulations, in *Tectonics, Climate and Landscape Evolution, Penrose Conference Series*, edited by S. Willett et al., *Spec. Pap. Geol. Soc. Am.*, *398*, 201–225, doi:10.1130/2006.2398(12).

Hubbert, M. (1937), Theory of scale models as applied to the study of geological structures, *Geol. Soc. Am. Bull.*, *48*, 1459–1520.

Hubert-Ferrari, A., J. Suppe, J. Van Der Woerd, X. Wang, and H. Lu (2005), Irregular earthquake cycle along the southern Tianshan front, Aksu area, China, *J. Geophys. Res.*, *110*, B06402, doi:10.1029/2003JB002603.

Jackson, J., J.-F. Ritz, L. Siame, G. Raisbeck, F. Yiou, R. Norris, J. Youngson, and E. Bennett (2002), Fault growth and landscape development rates in Otago, New Zealand, using in situ cosmogenic ^{10}Be, *Earth Planet. Sci. Lett.*, *195*(3–4), 185–193.

Jones, M. A., P. L. Heller, E. Roca, M. Garces, and L. Cabrera (2004), Time lag of syntectonic sedimentation across an alluvial basin: Theory and example from the Ebro Basin, Spain, *Basin Res.*, *16*(4), 467–488, doi:10.1111/j.1365-2117.2004.00244.x.

Khazaradze, G., A. Qamar, and H. Dragert (1999), Tectonic deformation in western Washington from continuous GPS measurements, *Geophys. Res. Lett.*, *26*(20), 3153–3156.

Koons, P. O., P. K. Zeitler, C. P. Chamberlain, D. Craw, and A. S. Meltzer (2002), Mechanical links between erosion and metamorphism in Nanga Parbat, Pakistan Himalaya, *Am. Sci.*, *302*(9), 749–773.

Kopp, C., J. Fruehn, E. Flueh, C. Reichert, N. Kukowski, J. Bialas, and D. Klaeschen (2000), Structure of the Makran subduction zone from wide-angle and reflection seismic data, *Tectonophysics*, *329*, 171–191.

Kopp, H., and N. Kukowski (2003), Backstop geometry and accretionary mechanics of the Sunda margin, *Tectonics*, *22*(6), 1072, doi:10.1029/2002TC001420.

Koyi, H. (1995), Mode of internal deformation in sand wedges, *J. Struct. Geol.*, *17*(2), 293–300.

Kukowski, N., S. E. Lallemand, J. Malavieille, M.-A. Gutscher, and T. J. Reston (2002), Mechanical decoupling and basal duplex formation observed in sandbox experiments with application to the Western Mediterranean Ridge accretionary complex, *Mar. Geol.*, *186*(1–2), 29–42.

Lavé, J., and J. Avouac (2000), Active folding of fluvial terraces across the Siwaliks Hills, Himalayas of central Nepal, *J. Geophys. Res.*, *105*, 5735–5770.

Le Pichon, X., S. J. Lallemant, N. Chamot Rooke, D. Lemeur, and G. Pascal (2002), The Mediterranean Ridge backstop and the Hellenic nappes, *Mar. Geol.*, *186*(1–2), 111–125.

Lohrmann, J., N. Kukowski, J. Adam, and O. Oncken (2003), The impact of analogue material properties on the geometry, kinematics, and dynamics of convergent sand wedges, *J. Struct. Geol.*, *25*(10), 1691–1711.

Malavieille, J. (1984), Modélisation expérimentale des chevauchements imbriqués: Application aux chaines de montagnes, *Bull. Soc. Geol. Fr.*, *7*, 129–138.

Mandl, G. (1988), *Mechanics of Tectonic Faulting*, 1 ed., Elsevier, New York.

Mandl, G., L. N. J. de Jong, and A. Maltha (1977), Shear zones in granular material; an experimental study of their structure and mechanical genesis, *Rock Mech.*, 95–144, Suppl. 9.

Marone, C. (1998), Laboratory-derived friction laws and their application to seismic faulting, *Annu. Rev. Earth Planet. Sci.*, *26*, 643–696.

Marshak, S. (2004), Salients, recesses, arcs, oroclines, and syntaxes: A review of ideas concerning the formation of map-view curves in fold-thrust belts, in *Thrust Tectonics and Hydrocarbon Systems*, edited by K. R. McClay, *AAPG Mem.*, *82*, 131–156.

Masaferro, J. L., M. Bulnes, J. Poblet, and G. P. Eberli (2002), Episodic folding inferred from syntectonic carbonate sedimentation: The Santaren anticline, Bahamas foreland, *Sediment. Geol.*, *146*(1–2), 11–24.

McClay, K. R., and P. S. Whitehouse (2004), Analog modeling of doubly vergent thrust wedges, in *Thrust Tectonics and Hydrocarbon Systems*, edited by K. R. McClay, *AAPG Mem.*, *82*, 184–206.

Meigs, A. J., J. Verges, and D. W. Burbank (1996), Ten-million-year history of a thrust sheet, *Geol. Soc. Am. Bull*, *108*, 1608–1625.

Molinaro, M., P. Leturmy, J.-C. Guezou, and S. A. Eshraghi (2005), The structure and kinematics of the southeastern Zagros fold-thrust belt, Iran: From thin-skinned to thick-skinned tectonics, *Tectonics*, *24*, TC3007, doi:10.1029/2004TC001633.

Moore, G. F., et al. (2001), New insights into deformation and fluid flow processes in the Nankai Trough accretionary prism: Results of Ocean Drilling Program Leg 190, *Geochem. Geophys. Geosyst.*, *2*(10), doi:10.1029/2001GC000166.

Moore, J., et al. (1991), EDGE deep seismic reflection transect of the eastern Aleutian arc- trench layered lower crust reveals underplating and continental growth, *Geology*, *19*, 420–424.

Morley, C. K. (1988), Out-of-sequence thrusts, *Tectonics*, *7*(3), 539–561.

Mulugeta, G., and H. Koyi (1992), Episodic accretion and strain partitioning in a model sand wedge, *Tectonophysics*, *202*, 319–333.

Naylor, M., H. D. Sinclair, S. Willett, and P. A. Cowie (2005), A discrete element model for orogenesis and accretionary wedge growth, *J. Geophys. Res.*, *110*, B12403, doi:10.1029/2003JB002940.

Norabuena, E., T. Dixon, S. Stein, and C. Harrison (1999), Decelerating Nazca-South America and Nazca-Pacific plate motions, *Geophys. Res. Lett.*, *26*(22), 3405–3408.

Okubo, C. H., and R. Schultz (2005), Evolution of damage zone geometry and intensity in porous sandstone: Insight gained from strain energy density, *J. Geol. Soc. London*, *162*, 939–949.

Oldow, J., L. Ferranti, D. Lewis, J. Campbell, B. Argenio, R. Catalano, G. Pappone, L. Carmignani, P. Conti, and C. Aiken (2002), Active fragmentation of Adria, the North African promontory, central Mediterranean Orogen, *Geology*, *30*, 779–782.

Oncken, O., A. Plesch, J. Weber, W. Ricken, and S. Schrader (2000), Passive margin detachment during arc-continental collision (central European Variscides), in *Orogenic Processes: Quantification and Modelling in the Variscan Belt*, edited by W. Franke et al., *Geol. Soc. Spec. Publ.*, *179*, pp. 199–216.

Pfiffner, O. A., S. Ellis, and C. Beaumont (2000), Collision tectonics in the Swiss Alps: Insight from geodynamic modeling, *Tectonics*, *19*, 1065–1094.

Platt, J. P. (1986), Dynamics of orogenic wedges and the uplift of high-pressure metamorphic rocks, *Geol. Soc. Am. Bull*, *97*, 1037–1053.

Platt, J. P. (1988), The mechnics of frontal imbrication: A first-order analysis, *Int. J. Earth Sci.*, *77*(2), 577–589.

Prawirodirdjo, L., Y. Bock, J. Genrich, S. Puntodewo, J. Rais, C. Subarya, and S. Sutisna (2000), One century of tectonic deformation along the Sumatran Fault from triangulation and Global Positioning System surveys, *J. Geophys. Res.*, *105*(12), 28,343–28,361.

Schäfer, F., O. Oncken, H. Kemnitz, and R. L. Romer (2000), Upper-plate deformation during collisional orogeny: A case study from the German Variscides (Saxo-Thuringian Zone), in *Orogenic processes; quantification and modelling in the Variscan Belt*, edited by W. Franke et al., *Geol. Soc. Spec. Publ.*, *179*, 281–302.

Schreurs, G., et al. (2006), Analogue benchmarks of shortening and extension experiments, in *Analogue and Numerical Modelling of Crustal-Scale Processes*, edited by S. Buiter and G. Schreurs, *Geol. Soc. Spec. Publ.*, *253*, 1–27.

Seno, T., S. Stein, and A. Gripp (1993), A model for the motion of the Philippine Sea Plate consistent with NUVEL-1 and geological data, *J. Geophys. Res.*, *98*(10), 17,941–17,948.

Silver, E. A., and D. L. Reed (1988), Backthrusting in accretionary wedges, *J. Geophys. Res.*, *93*, 3116–3126.

Speed, R. (1990), Volume loss and defluidization history of Barbados, *J. Geophys. Res.*, *95*, 8983–8996.

Storti, F., F. Salvini, and K. R. McClay (2000), Synchronous and velocity-partitioned thrusting and thrust polarity reversal in experimentally produced, doubly-vergent thrust wedges: Implications for natural orogens, *Tectonics*, *19*, 378–396.

Taira, A., I. A. Hill, and J. V. Firth (1991), *Proceedings, Initial Reports, Ocean Drilling Program*, vol. 131, Ocean Drill. Program, Tex. A and M Univ., College Station.

Tozer, R., R. Butler, and S. Corrado (2002), Comparing thin- and thick-skinned thrust tectonic models of the central Apennines, Italy, in *Continental Collision and the Tectono-sedimentary Evolution of Forelands*, *Stephan Mueller Spec. Publ. Ser.*, vol. 1, edited by G. Bertotti, K. Schulmann, and S. A. P. L. Cloetingh, pp. 181–194, Eur. Geosci. Union, Vienna, Austria.

Travé, A., F. Calvet, M. Sans, J. Verges, and M. Thirlwall (2000), Fluid history related to the Alpine compression at the margin of the South-Pyrenean foreland basin: The El Guix anticline, *Tectonophysics*, *321*, 73–102.

Vernant, P., et al. (2004), Present-day crustal deformation and plate kinematics in the Middle East constrained by GPS measurements in Iran and northern Oman, *Geophys. J. Int.*, *157*(1), 381–398.

von Huene, R., D. Klaeschen, M. Gutscher, and J. Fruehn (1998), Mass and fluid flux during accretion at the Alaskan margin, *Geol. Soc. Am. Bull*, *110*, 468–482.

Wang, W. H., and D. M. Davis (1996), Sandbox model simulation of forearc evolution and noncritical wedges, *J. Geophys. Res.*, *101*, 11,329–11,339.

Willett, S. D. (1999), Orogeny and orography; the effects of erosion on the structure of mountain belts, *J. Geophys. Res.*, *104*, 28,957–28,982.

Willett, S., C. Beaumont, and P. Fullsack (1993), Mechanical model for the tectonics of doubly vergent compressional orogens, *Geology*, *21*, 371–374.

Willett, S. D., R. Slingerland, and N. Hovius (2001), Uplift, shortening, and steady state topography in active mountain belts, *Am. Sci.*, *301*(4–5), 455–485.

Wojtal, S., and G. Mitra (1986), Strain hardening and strain softening in fault zone from foreland thrusts, *Geol. Soc. Am. Bull.*, *97*, 674–687.

Yu, S.-B., H.-Y. Chen, and L.-C. Kuo (1997), Velocity field of GPS stations in the Taiwan area, *Tectonophysics*, *274*, 41–59.

Yue, L., J. Suppe, and J. Hung (2005), Structural geology of a classic thrust belt earthquake: The 1999 Chi-Chi earthquake Taiwan (m_w = 7.6), *J. Struct. Geol.*, *27*(11), 2058–2083, doi:10.1016/j.jsg.2005.05.020.

Zachos, J., H. Pagani, L. Sloan, E. Thomas, and K. Billups (2001), Trends, rhythms, and aberrations in global climate 65 Ma to present, *Science*, *292*(5517), 686–693, doi:10.1126/science.1059412.

Zeitler, P. K., et al. (2001), Crustal reworking at Nanga Parbat, Pakistan: Metamorphic consequences of thermal-mechanical coupling facilitated by erosion, *Tectonics*, *20*, 712–728.

A. Hoffmann-Rothe, Bundesanstalt für Geowissenschaften und Rohstoffe, Stilleweg 2, D-30655 Hannover, Germany. (ahoro@bgr.de)

S. Hoth and N. Kukowski, GeoForschungsZentrum Potsdam, Telegrafenberg, D-14473 Potsdam, Germany. (shoth@gfz-potsdam.de; nina@gfz-potsdam.de)